Original Paper

Eletrônica de Potência
Open Journal of Power Electronics

Received November 08, 2025; Received in revised form January 06, 2026; Accepted January 17, 2026; Date of publication January 28, 2026.
The review of this paper was arranged by Associate Editor Janaína G. de Oliveira and Editor-in-Chief Allan F. Cupertino.
*Digital Object Identifier http://doi.org/10.18618/REP.e202609*

# An Optimized Hybrid FOPID+RMRAC Control Architecture for Grid-tied Inverters with LCL Filters

**Cairo T. G. B. Oliveira[1], Wagner B. da Silveira[2], Paulo J. D. de O. Evald[1,*]**

[1]Federal University of Pelotas, Intelligent Systems and Control Group, Pelotas – RS, Brazil.
[2]Federal University of Santa Maria, Group of Power Electronics and Control, Santa Maria – RS, Brazil.

e-mail: cairo.tulio@ufpel.edu.br; wagner.silveira@acad.ufsm.br; paulo.evald@ufpel.edu.br*.
*Correspondig author.

**ABSTRACT** This paper presents a novel hybrid control architecture for grid-tied inverters with an LCL filter, combining a fractional-order proportional-integral-derivative controller, dedicated to reference tracking, and a robust model reference adaptive controller, employed for active rejection of grid disturbances. A systematic tuning procedure using the puma optimizer is provided to tune all eleven parameters of the composed control algorithm. Experimental results, performed on a TMS320F28335 Delfino microcontroller equipped in a laboratory prototype, corroborate the simulation findings, presenting fast current tracking and disturbance rejection, with low settling time and total harmonic distortion below the limits established by the IEEE 1547 standard, whose mean between the three-phases is 2.55% in steady state.

**KEYWORDS** Adaptive control, Current controller, Metaheuristic optimization, VSI.

## I. INTRODUCTION

The growing global energy demand, sustained mainly by fossil fuels, has intensified greenhouse gas emissions (GHG), culminating in an unprecedented climate crisis [1]. Extreme climate events, biodiversity loss, and risks to human health are direct consequences of this interference in the environmental balance [2]. International agreements such as the Paris Agreement establish ambitious targets for emissions reduction, aiming to limit global warming. Intergovernmental Panel on Climate Change (IPCC) reports indicate the need for drastic reductions in GHG emissions in the coming decades to achieve these objectives [3], making the transition to a clean energy matrix a necessity.

In this scenario, renewable energy sources stand out as the most viable solution to decarbonize the power sector. The installed capacity of these sources has grown exponentially on a global scale, representing the vast majority of new power generation additions [4]. The fundamental link between these sources and the electrical grid are the power electronic converters, typically voltage source inverters (VSIs). To ensure the quality and safety of the energy injected into the grid, passive filters are indispensable for attenuating the high-frequency harmonics generated by the inverter switching [5]. Among the filter topologies, L and LCL filters are commonly used, being the second one the most popular due to its high attenuation capability, reduced size, and competitive cost [6].

Despite its advantages, the LCL filter introduces a resonance peak in the system's frequency response [7], a notorious challenge that can lead to instability if not duly treated [8]. The active damping technique, in which the current controller itself is designed to mitigate this resonance, is the preferred approach as it avoids the power losses inherent in passive damping methods [9]. The challenge intensifies considering that the grid impedance is not constant nor precisely known, which can shift the resonance frequency and degrade the linear fixed-gain controllers performance.

Traditionally, proportional-integral-derivative (PID) controllers are the first choice in many industrial applications. However, their structure with only three degrees of freedom can be insufficient for the precise control of systems with complex coupled dynamics and relevant disturbances, as is the case of inverters with LCL filters. To overcome this limitation, fractional-order PID (FOPID) controllers, originally proposed by [10], emerged as a more suitable alternative. By introducing the integrator ($\lambda$) and differentiator ($\mu$) orders as tuning parameters, the FOPID expands the control plane from points (P, PI, PD, PID) to a continuous plane, offering five degrees of freedom ($K_p, K_i, K_d, \lambda, \mu$). This additional flexibility allows for a much finer adjustment of the dynamic response, enabling more precise and robust control. However, even a well-tuned FOPID still operates with fixed gains, making it vulnerable to disturbances and parametric variations not foreseen in the design.

A natural solution would be the development of adaptive FOPID controllers. Recent literature indeed explores several strategies, using fuzzy logic [11], neural networks [12], [13], neurofuzzy [14], and sliding mode control (SMC) [15], SMC and fuzzy logic [16], and sigmoids [17]. Although effective, these approaches often result in complex adaptation laws, which results in high computational burden.

In this context, this work presents a novel control architecture combining the high performance of the FOPID for

fast tracking with the robustness of a robust model reference adaptive controller (RMRAC) for disturbance rejection. Both controllers are optimized using a meta-heuristic algorithm to extract its maximum performance. The resulting structure, named FOPID+RMRAC, combines the flexibility of the FOPID with the robustness and adaptation capability of the RMRAC in a parallel action, keeping the implementation complexity reduced. The developed controller is experimentally implemented for grid-injected current regulation of a three-phase VSI with an LCL filter, subject to reference variations and abrupt changes in the electrical grid parameters. The main contributions of this work are:

- A novel FOPID+RMRAC controller;
- A systematic procedure to tune the eleven parameters of FOPID+RMRAC using the puma optimizer (PO) [18]
- Experimental validation of the developed control strategy in a laboratory prototype.

## II. PLANT DESCRIPTION AND MODELING

Figure 1 depicts the closed-loop system, which consists of a three-phase VSI connected to the electrical grid through an LCL filter, where $L_c$, $C_f$, and $L_{g1}$ are the LCL filter parameters. Furthermore, $v_d$ and $v_{link}$ are the grid voltage and the DC link voltage. Besides, $r_c$, $r_{g1}$, and $r_{g2}$ are the parasitic resistances. The line-to-line voltages ($V_{ab}$ and $V_{bc}$) are measured at the point of common coupling (PCC) and used for VSI synchronization through a Kalman filter [19], implemented in digital signal processing (DSP), where the controller runs and is synthesized utilizing the space vector modulation (SVM).

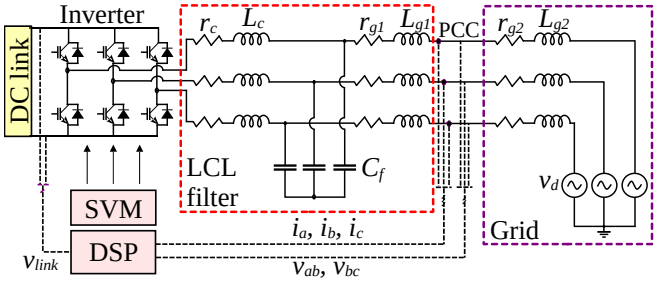


**FIGURE 1. Three-phase grid-tied VSI with an LCL filter.**

The system dynamics are represented by the relationship between the grid-injected current ($i_g$) and the output voltage modulated by the inverter ($V_{inv}$). Assuming a balanced system and applying the Clarke transform to decouple the phases, the equivalent single-phase model is [20]:

$$\frac{i_g(s)}{V_{inv}(s)} = \frac{\frac{1}{L_g L_c C}}{s^3 + \frac{(R_g L_c + R_c L_g)}{L_g L_c} s^2 + \frac{(L_c + L_g + R_g R_c C)}{L_g L_c C} s + \frac{R_g + R_c}{L_g L_c C}}, \quad (1)$$

The LCL filter parameters are $L_c$ = 1 mH, $C_f$ = 62 $\mu$F, $L_{g1}$ = 0.3 mH [21], while the grid parameters are $v_d$ = 127 $V_{rms}$/60 Hz with 0.3 mH (or 1.3 mH during parametric variation test). Yet, the sampling and switching frequencies are 5040 Hz, while $r_c$, $r_{g1}$, and $r_{g2}$ are considered 50 m$\Omega$.

## III. FOPID+RMRAC CONTROLLER

Next, the theory of each control algorithm is discussed.

### A. FOPID controller

The FOPID controller is a generalization of the classic PID controller, introduced by [10], which uses fractional-order calculus operators for the integral and derivative actions. The FOPID control action $u_{FOPID}$ is described by the following fractional-order differential equation [22]:

$$u_{FOPID}(t) = K_p e(t) + K_i \mathcal{D}^{-\lambda} e(t) + K_d \mathcal{D}^{\mu} e(t), \quad (2)$$

where $e(t)$ is the tracking error, while $K_p$, $K_i$, and $K_d$ are the proportional, integral, and derivative gains, respectively. Besides, $\lambda$ and $\mu$ are the orders of the fractional integrator and differentiator, respectively. The five tuning parameters $(K_p, K_i, K_d, \lambda, \mu)$ offer superior flexibility compared to the traditional PID, however, the implementation of fractional operators in a digital controller requires an integer-order approximation. Therefore, the Oustaloup approximation is adopted for digital implementation of FOPID.

### B. Oustaloup Approximation

For the digital implementation of the FOPID, the fractional operators $s^{\mu}$ (derivative) and $s^{-\lambda}$ (integral) are approximated by the recursive Oustaloup technique [23]. This method approximates the fractional-order operator $s^{\alpha}$ by an integer-order filter $N_o$ in a defined frequency range $[\omega_L, \omega_H]$. The continuous transfer function of the Oustaloup filter is

$$s^{\nu} \approx K_{of} \prod_{n=1}^{N_o} \frac{1 + s/\omega_{z,n}}{1 + s/\omega_{p,n}}, \quad (3)$$

where $K_{of}$ is an adjustable gain, while $\omega_{z,n}$ and $\omega_{p,n}$ are the frequencies of the $N_o$ zeros and $N_o$ poles of the filter, respectively. These frequencies are logarithmically distributed in the range $[\omega_L, \omega_H]$ and recursively calculated to approximate the frequency response of the fractional operator, as follows:

$$K_{of} = \omega_H^{\nu}, \quad (4)$$

$$\omega_{z,1} = \omega_L \sqrt{\eta}, \quad (5)$$

$$\omega_{p,n} = \omega_{z,n} \alpha, \quad \text{for } n = 1, ..., N_o, \quad (6)$$

$$\omega_{z,n+1} = \omega_{p,n} \eta, \quad \text{for } n = 1, ..., N_o - 1, \quad (7)$$

with the terms $\alpha$ and $\eta$ being dependent on the frequency limits and the fractional order $\nu$:

$$\alpha = \left(\frac{\omega_H}{\omega_L}\right)^{\nu/N_o} \text{ and } \eta = \left(\frac{\omega_H}{\omega_L}\right)^{(1-\nu)/N_o}. \quad (8)$$

After discretization via the Tustin transform, each fractional operator is implemented as a recursive digital filter. Thus, the integral and derivative parts of the control action

are calculated as the output of their respective Oustaloup filters, taking the error $e(k)$ as input:

$$I_\lambda(k) = \text{Oustaloup}\{e(k), b_\lambda, a_\lambda\}, \tag{9}$$
$$D_\mu(k) = \text{Oustaloup}\{e(k), b_\mu, a_\mu\}, \tag{10}$$

where $b_\lambda, a_\lambda$ are the coefficients for the $s^{-\lambda}$ operator and $b_\mu, a_\mu$ are for the $s^\mu$ operator. The final discrete FOPID control action is composed of the sum of the proportional part and the outputs of the fractional filters:

$$u_{FOPID}(k) = K_p e(k) + K_i I_\lambda(k) + K_d D_\mu(k). \tag{11}$$

### C. RMRAC

The RMRAC structure is based on a gradient adaptation law that adjusts the controller gains in real-time as demonstrated in [24]. However, it is utilized exclusively the terms related to disturbance rejection. Therefore, the grid disturbance is decomposed into phase $V_s(k)$ and quadrature $V_c(k)$ components. The control action for disturbance rejection is $u_d(k) = -[\theta_c(k)V_c(k)+\theta_s(k)V_s(k)]$, where $\theta_s(k)$ and $\theta_c(k)$ are adaptive gains.

The gradient adaptation law, which updates these gains is

$$\boldsymbol{\theta_d}(k+1) = \boldsymbol{\theta_d}(k) - T_s\sigma(k)\boldsymbol{\Gamma\theta_d}(k) - \frac{T_s\boldsymbol{\Gamma}\kappa\boldsymbol{\omega}(k)e_0(k)}{\bar{m}^2(k)}, \tag{12}$$

where $\boldsymbol{\theta_d}(k) = [\theta_c(k)\ \theta_s(k)]$, $\boldsymbol{\omega}(k) = [V_s(k)\ V_s(k)]$, $T_s$ is the sampling period, $\boldsymbol{\Gamma}$ is the adaptation rate matrix, and $\kappa$ is a positive constant. Besides, the tracking error is $e_0(k) = r(k) - y(k)$. To ensure robustness, the adaptation law includes two mechanisms: the majorant signal $\bar{m}^2(k)$ and the $\sigma$-modification $\sigma(k)$. The majorant signal is

$$\bar{m}^2(k) = m_2^2(k) + \boldsymbol{\omega}^T(k)\boldsymbol{\Gamma\omega}(k), \tag{13}$$

where $m_2^2(k)$ is an auxiliary dynamic signal updated by:

$$m_2^2(k) = (1-\delta_0 T_s)m_2^2(k-1) + \delta_1 T_s(1+|y(k)|+|u_d(k)|), \tag{14}$$

with $\delta_0$ and $\delta_1$ being positive design constants.

The $\sigma$-modification is

$$\sigma(k) = \begin{cases} 0 & \text{if } ||\theta_d(k)|| < M_0 \\ \sigma_0\left(\frac{||\theta_d(k)||}{M_0} - 1\right) & \text{if } M_0 \le ||\theta_d(k)|| < 2M_0, \\ \sigma_0 & \text{if } ||\theta_d(k)|| \ge 2M_0 \end{cases} \tag{15}$$

where $\sigma_0$ is a positive constant.

### D. The FOPID+RMRAC strategy

The developed approach consists of a complementary parallel control architecture, in which each one performs a specific task. In this sense, the total control action $u(k) = u_{FOPID}(k) + u_d(k)$ applied to the inverter is the sum of the outputs from both controllers. Figure 2 depicts the block diagram of the FOPID+RMRAC.

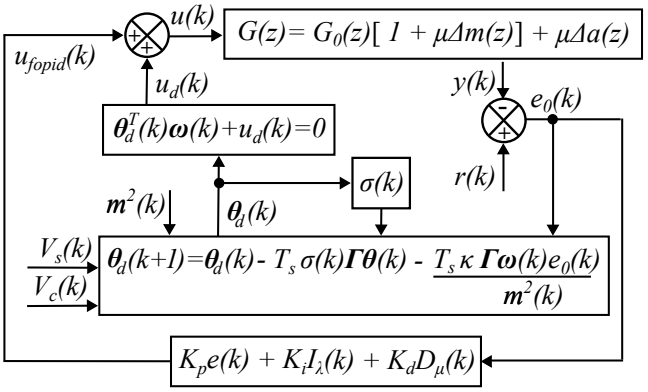


**FIGURE 2. Block diagram of the FOPID+RMRAC.**

### E. Optimization Procedure

The parameter tuning for the proposed control architecture is a complex task due to the high number of variables (eleven in total), which encompass both the FOPID and RMRAC, already considering some previous well-established parameters of RMRAC-based controllers from literature. Therefore, to automate and find an optimal set of parameters, the puma optimizer [18], PO, was employed for this task. The PO's objective is to find the parameter vector $S$ that minimizes a given cost function (or *fitness*). To do this, systematic rules were drawn, tailored specifically for the grid-injected current controller of a grid-tied VSI with an LCL filter. The search vector $S$ is $S = [K_p, K_i, K_d, \lambda, \mu, N_o, \omega_L, \Gamma, \kappa, \theta_c(0), \theta_s(0)]$, where the first five parameters belong to the FOPID, while $N_o$ and $\omega_L$ are from the Oustaloup approximation, and the last four are the parameters and initial gain values of the RMRAC. The search space of each parameter is limited by lower bound ($lb$) and upper bound ($ub$)

$$\begin{aligned} \boldsymbol{lb} &= [0, 1, 0, 0, 0, 1, 0, 1, 1, -1, -1] \\ \boldsymbol{ub} &= [1, 2, 1, 2, 2, 20, 1000, 100, 100, 1, 1]. \end{aligned} \tag{16}$$

The cost function was defined as the mean absolute error (MAE), which offers a direct measure of the average magnitude of the tracking errors. Additionally, to ensure that the found solutions are physically realizable and safe for the hardware, a penalty function was added to the optimization routine. It consists in evaluating if the maximum control action exceeds the inverter's voltage limits (e.g., $|u(k)| > 500$ V). Solutions that violated this constraint received an extremely high cost value ($10^4$), being discarded by the algorithm. Besides, PO was configured with 30 pumas and 500 iterations. Other controller parameters, such as the upper frequency of the Oustaloup approximation ($\omega_H$ = 77000 rad/s) and the RMRAC robustness parameters ($\sigma_0 = 0.1, M_0 = 4, \delta_0 = 0.7$, and $\delta_1$=1), were kept fixed during optimization, with values established based on the literature of RMRAC-based controllers [7], [21], [25].

## IV. SIMULATION RESULTS

Numerical simulations were performed in the MATLAB® environment. The proposed architecture is compared with a benchmark integer-order PI combined with the RMRAC (PI+RMRAC), which was tuned using PO to ensure a fair assessment. Figure 3 presents the comparative response of grid-injected currents, control actions, and tracking errors under three scenarios: initial transient, parametric variation ($t = 0.17$ s), and load step change ($t = 0.24$ s). The corresponding quantitative metrics are summarized in Table 1, with the best results highlighted in bold. Although the PI+RMRAC exhibits a slightly smaller overshoot during Phase 1, the FOPID+RMRAC demonstrates superior robustness against exogenous disturbances and uncertainties. This is evident during Phase 2, where the grid inductance increases from 0.3 mH to 1.3 mH. In this critical scenario, the proposed controller restricts the overshoot to 10.12%, whereas the benchmark reaches 40.25%. Similarly, during Phase 3, the FOPID+RMRAC reduces the settling time by approximately 62% compared to the PI+RMRAC.

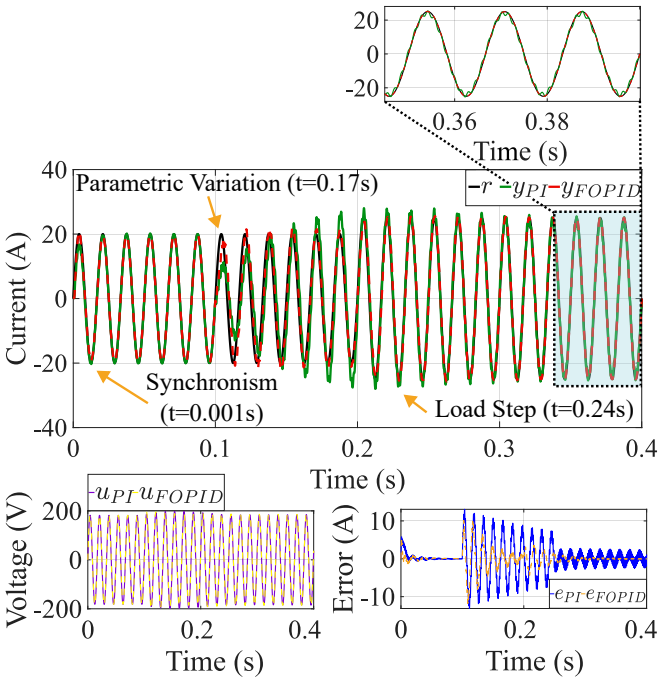


**FIGURE 3. Simulation results.**

## V. EXPERIMENTAL RESULTS

Experimental tests were conducted on a 6.75 kW laboratory test bench. The control strategy was implemented on a TMS320F28335 DSP microcontroller from Texas Instruments. Figure 4 illustrates the experimental setup. The experimental protocol was designed to evaluate the controller performance similar to those discussed in the simulation. The test begins with a current reference of 20 A. At $t \approx 0.17$ s, a parametric variation is induced, increasing the grid inductance to simulate an abrupt weakening, changing grid inductance from 0.3 mH to 1.3 mH. A weak grid (high impedance) increases the risk of instability, being a suitable test to verify the controller's robustness. Subsequently, at $t \approx 0.24$ s, a reference step is applied, raising the current to 25 A. The nominal controller parameters are summarized in Table 2. As the system is assumed to be balanced, the controllers are identical for $\alpha$ and $\beta$ coordinates.

**TABLE 1. Performance comparison.**

| Category | Metric | FOPID+RMRAC | PI+RMRAC |
|---|---|---|---|
| Error metrics | MAE | **1.0754** | 2.6421 |
| | MSE | **4.4886** | 16.4066 |
| | RMSE | **2.1186** | 4.0505 |
| | IAE | **0.4318** | 1.0584 |
| | ISE | **1.8049** | 6.5719 |
| | ITAE | **0.0652** | 0.1953 |
| | ITSE | **0.2313** | 1.0647 |
| *Transient analysis by event* | | | |
| Phase 1: initial transient (Ref: 20 A) | Overshoot (%) | 3.57 | **1.08** |
| | Settling time (s) | 0.0133 | **0.0101** |
| Phase 2: parametric Variation | Overshoot (%) | **10.12** | 40.25 |
| | Settling time (s) | **0.0986** | 0.1500 |
| Phase 3: Change of reference (Ref: 20 A → 25 A) | Overshoot (%) | **2.74** | 11.82 |
| | Settling time (s) | **0.0562** | 0.1494 |

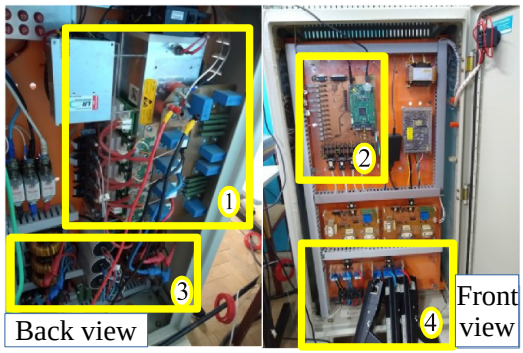


**FIGURE 4. Experimental setup used for controller validation: (1) VSI inverter, (2) DSP, (3) LCL filter, and (4) Current sensors.**

Figure 5 presents the reference tracking throughout the entire experiment. Visually, it is observed that the controller maintains fast tracking, even during transient events. More detail about transient regimes are given next. The computational burden related to the controller was 16.69 $\mu$s.

Figure 6 shows the tracking errors during the overall experiment, where the peaks are concentrated at the disturbance instants, with the system quickly converging to a low residual error in steady-state. The maximum observed error in the $\alpha$ coordinate was 7.40 A, while in the $\beta$ coordinate it was 20.92 A during the initial transient due to the delay relative to the $\alpha$ coordinate being quickly attenuated.

**TABLE 2. Controller parameters for the $\alpha$ and $\beta$ coordinates.**

| Parameter | Value | Parameter | Value |
|---|---|---|---|
| $K_p$ | 0.0 | $\Gamma$ | 100 |
| $K_i$ | 2.0 | $\kappa$ | 100 |
| $K_d$ | 0.0 | $\theta_{\alpha,\beta}(0)$ | $\begin{bmatrix}-0.0513655\\-1.0\end{bmatrix}$ |
| $\lambda$ | 0.137128 | $N_o$ | 1 |
| $\mu$ | 0.188004 | $\omega_L$ | 28.7444 rad/s |

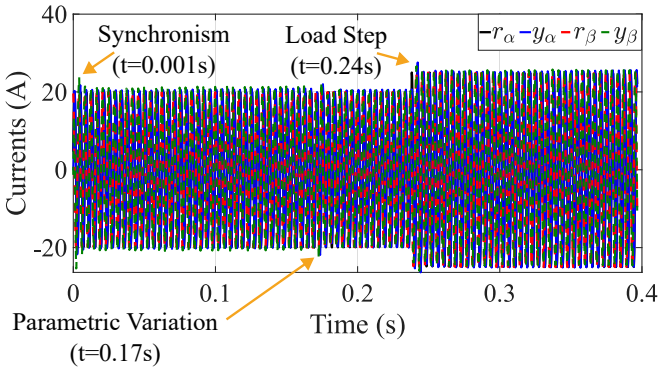


**FIGURE 5. Grid-side currents in $\alpha\beta$.**

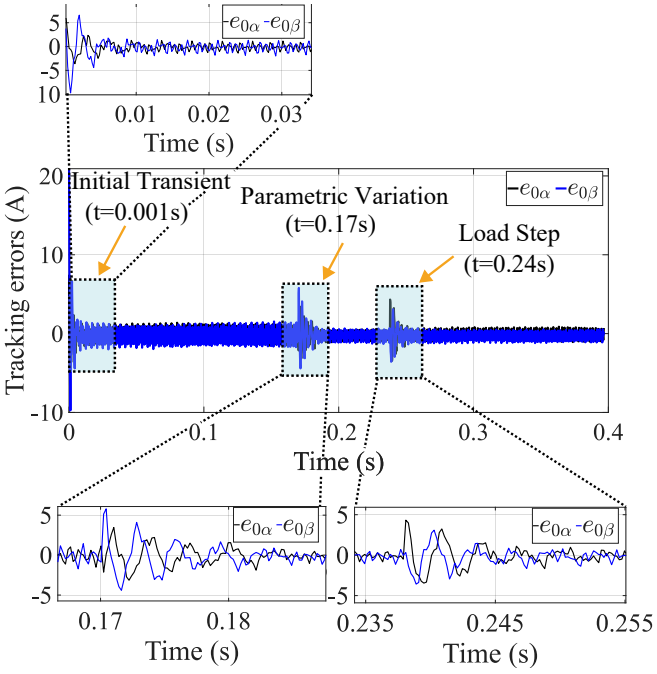


**FIGURE 6. Tracking errors.**

Figures 7 and 8 detail the adaptation of the RMRAC gains. At the beginning of the experiment ($t \approx 0.001$ s), the gains quickly adjust from their initial values to compensate for the real grid conditions. In each subsequent event (parametric variation and reference step), the gains readapt to find a new optimal operating point, demonstrating the effectiveness of the adaptation law. If not optimized, it could result in greater overshoots, leading to the VSI disconnection.

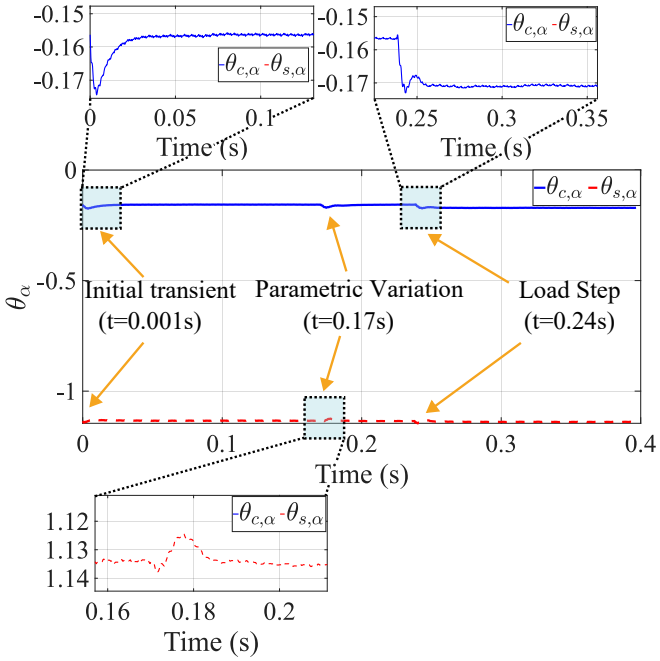


**FIGURE 7. Adaptation of gains in $\alpha$ coordinate.**

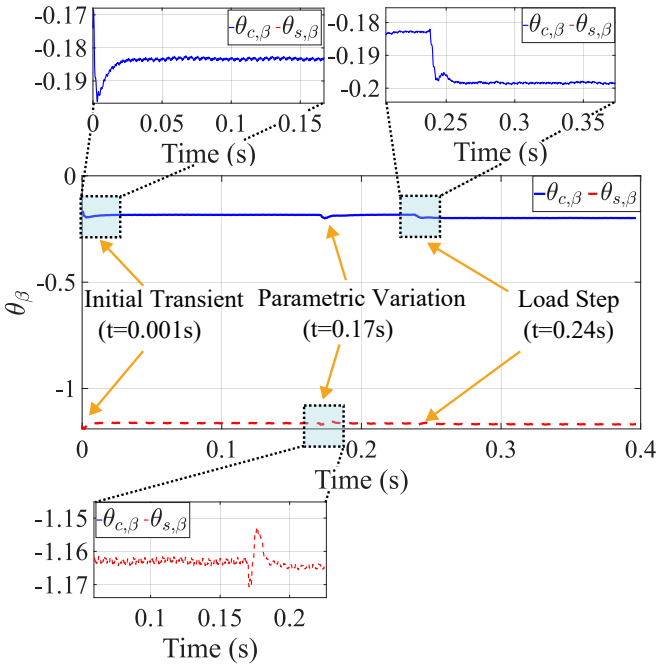


**FIGURE 8. Adaptation of gains in $\beta$ coordinate.**

Detailing further the tracking of reference currents, at startup (Figure 9), the controller presents an overshoot of 1.74 A (8.7%), which is a small tracking error for this critical

event of synchronization. During the parametric variation (Figure 10), the system exhibits notable robustness: the overshoot is contained at 1.99 A (9.95%), which is slightly higher, but the system recovers it in only 29 ms. Note that, although there is a long initial transient regime, this kind of event will occur only a few times, being predominantly the events of reference change and parametric variation in practice. Notably, its performance for dealing with grid inductance change was satisfactory.

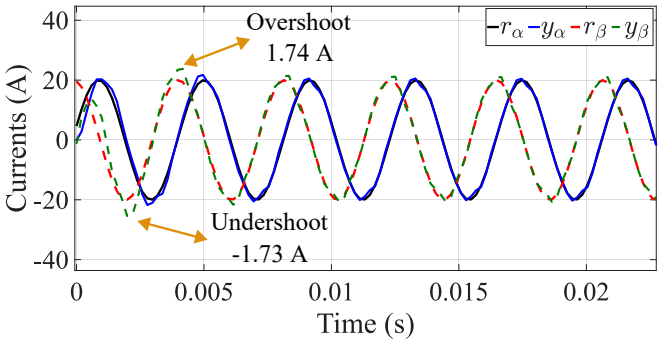


**FIGURE 9. Grid-side currents in $\alpha\beta$ (initial transient).**

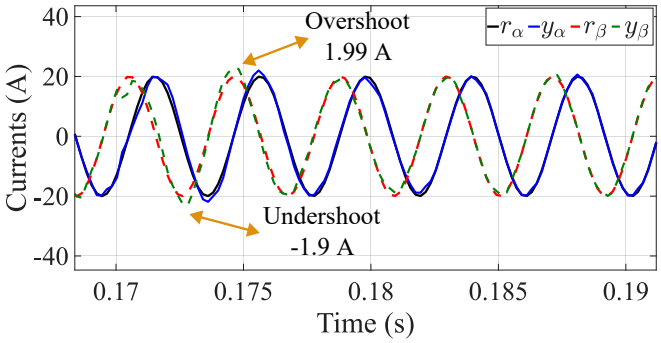


**FIGURE 10. Grid-side currents in $\alpha\beta$ (parametric variation).**

Figure 11 presents the current tracking during reference change. In response to this event, the controller demonstrates great agility, with a settling time of only 10.9 ms and an overshoot of 2.58 A (10.32%). Therefore, it can be affirmed that the controller is feasible for actuating under uncertain grid conditions and variable current reference, for injection of desired levels of active power.

Figure 12 shows the current tracking at steady-state. This zoom reveals the precision of the reference current tracking by the measured currents in steady state. The absence of significant oscillations and the maintenance of a minimal residual error are observed, demonstrating the FOPID+RMRAC's ability to keep the system stable, with fast current tracking, and appropriate disturbance rejection. Harmonic content is discussed next.

Figure 13 shows the control actions in $\alpha\beta$ and the DC bus voltage ($V_{cc}$). The maximum controller actuation was 146.68 V and 147.61 V in the $\alpha$ and $\beta$ coordinates, respectively. These values are well below the DC bus limit, 29.73% and 29.52% of the available DC link voltage, respectively. It confirms experimentally the implementation feasibility without risk of controller saturation.

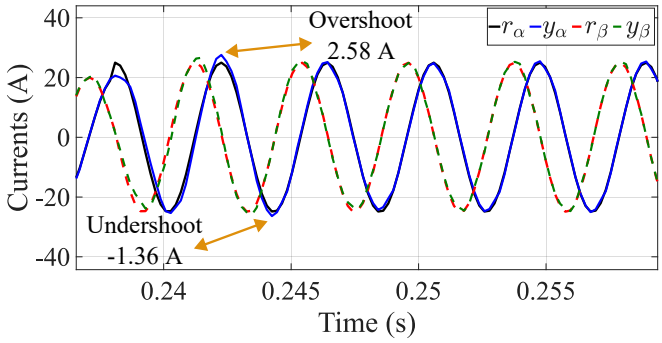


**FIGURE 11. Grid-side currents in $\alpha\beta$ at reference change.**

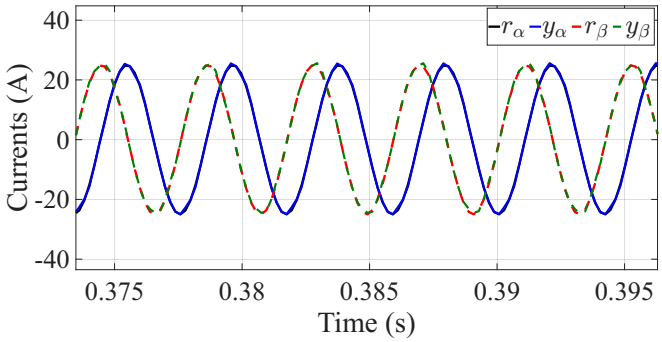


**FIGURE 12. Grid-injected currents in $\alpha\beta$ (steady state).**

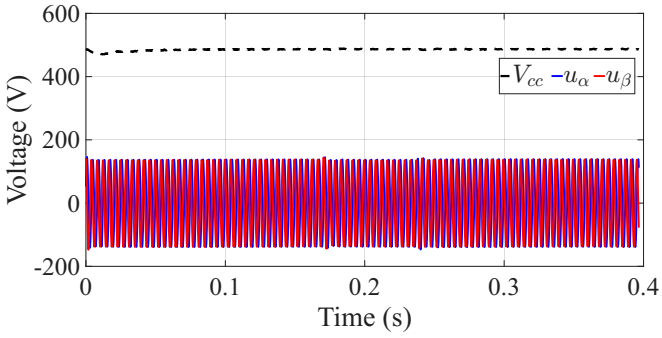


**FIGURE 13. DC link voltage and control actions in $\alpha\beta$.**

As a complement to the analysis of the data extracted from the DSP buffer, Figure 14 presents the three-phase currents injected into the grid ($i_a, i_b, i_c$), captured directly from the oscilloscope. The waveforms exhibit a high-quality sinusoidal profile, with low visible distortion, confirming in practice that the FOPID+RMRAC effectively regulates the

grid-injected currents, even under the conditions of a real grid with its inherent challenges.

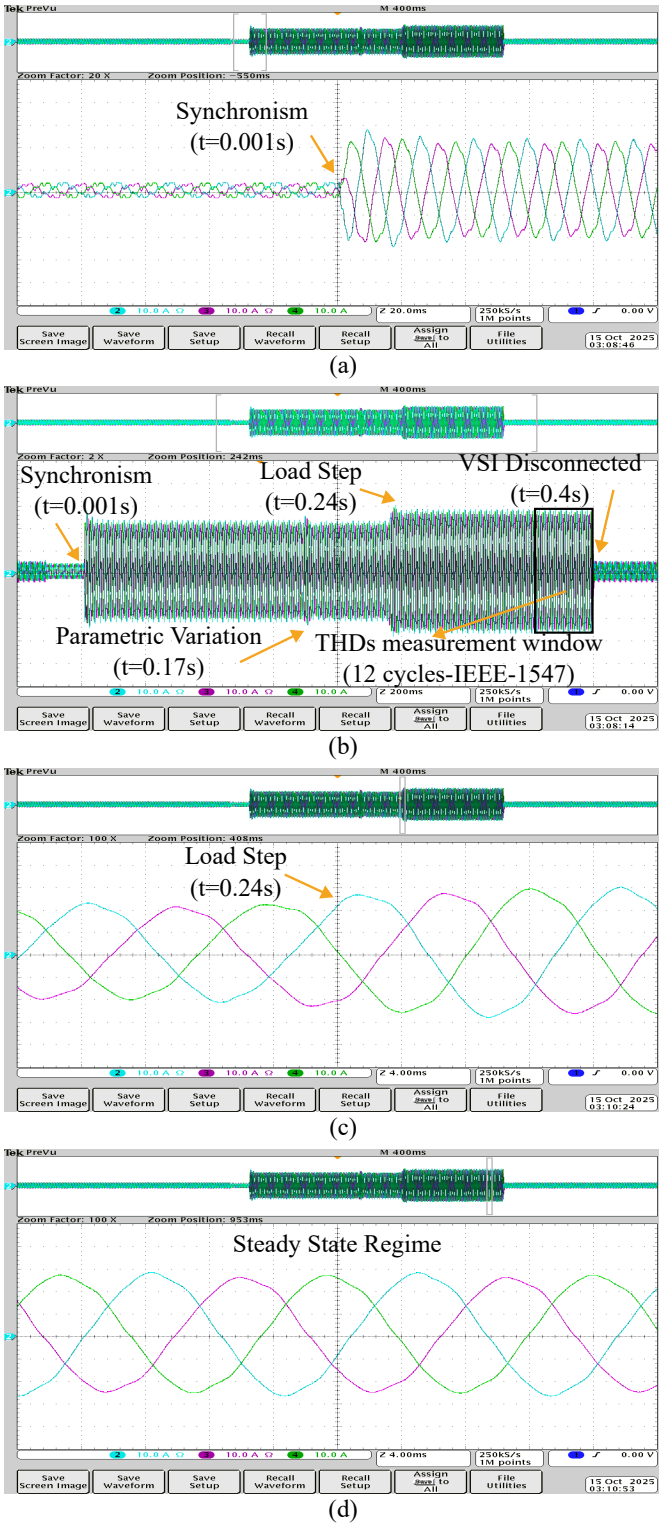


**FIGURE 14. Three-phase grid-side currents.**

Figure 15 shows the average total harmonic distortion (THD) of the three-phase currents in steady state, whose 12 cycle window was highlighted in the previous figure. The individual THDs for each phase were 2.46% (phase A), 2.85% (phase B), and 2.35% (phase C), resulting in a mean THD of 2.55%. Moreover, all individual harmonic components remain below the limits established by the IEEE 1547 standard. The presented figure evidences the first 50 harmonics of these currents. As can be observed, the currents are securely inside the accepted individual harmonic limits, validating the controller performance.

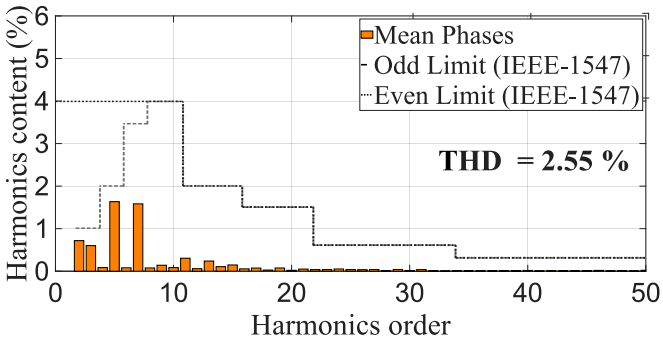


**FIGURE 15. Average harmonic distortion rate.**

## VI. CONCLUSION

This work presented a novel control architecture for grid-tied inverters, combining a FOPID controller with an RM-RAC. The developed approach ensures fast current reference tracking during reference changes and grid-inductance variation, while ensuring robustness and disturbance rejection. Additionally, a systematic procedure for controller tuning, based on a meta-heuristic optimizer was provided. Experimental results corroborated the feasibility and fast tracking of the FOPID+RMRAC, whose transient regime for current reference change and parametric variation were 10.9 ms (with overshoot of 2.58 A) and 29 ms (with overshoot of 2 A), respectively. The average THD of the grid-injected currents in steady state was 2.55%, meeting the requirements of the IEEE 1547 standard. Moreover, the required voltage to synthesize the control action in $\alpha$ and $\beta$ coordinates were 29.73% and 29.52% of the available voltage, respectively, which indicates securely the feasibility of practical implementation. Therefore, the FOPID+RMRAC is a robust controller, capable of operating with satisfactory performance for considered application, which is common in renewable energy systems.

## REFERENCES

[1] A. Raihan, "A review of the global climate change impacts, adaptation strategies, and mitigation options in the socio-economic and environmental sectors", *Journal of Environmental Science and Economics*, vol. 2, no. 3, pp. 36–58, Sep. 2023, doi:10.56556/jescae.v2i3.587.

[2] K. Wudu, A. Abegaz, L. Ayele, M. Ybabe, "The impacts of climate change on biodiversity loss and its remedial measures using nature based conservation approach: a global perspective", *Biodiversity and Conservation*, vol. 32, no. 12, pp. 3681–3701, Jul. 2023, doi:10.1007/s10531-023-02656-1.

[3] IPCC, "Climate Change 2023: Synthesis Report", https://www.ipcc.ch/report/ar6/syr/, accessed: 2025-03-04, 2024.

[4] REN21, "Renewables 2024 Global Status Report Collection - Global Overview", https://www.ren21.net/gsr-2024/modules/global_overview, accessed: 2025-03-04, 2024.

[5] G. V. Hollweg, P. J. D. O. Evald, G. G. Koch, E. Mattos, R. V. Tambara, H. A. Gründling, "Reference Model-based Robust Adaptive Super-Twisting Sliding Mode Controller for Weak Grid-Currents Regulation of Three-PhaseInverters with LCL Filter (*in portuguese*)", *Open Journal of Power Electronics*, vol. 26, no. 2, pp. 147–158, Jun. 2021, doi:10.18618/REP.2021.2.0001.

[6] G. V. Hollweg, P. J. D. O. Evald, R. V. Tambara, R. Z. Azzolin, H. A. Grundling, M. L. Martins, "Grid-tied photovoltaic quasi-Z-source inverter with LCL filter using a simplified MRAC-SM cascade structure for weak grids (*in portuguese*)", *Open Journalof Power Electronics*, vol. 26, no. 2, pp. 205–216, Jun. 2021, doi:10.18618/REP.2021.2.0069.

[7] P. J. D. O. Evald, G. V. Hollweg, R. V. Tambara, H. A. Gründling, "A discrete-time robust adaptive PI controller for grid-connected voltage source converter with LCL filter", *Open Journal of Power Electronics*, vol. 26, no. 1, pp. 19–30, Mar. 2021, doi:10.18618/REP.2021.1.0053.

[8] M. S. da Silva, G. V. Hollweg, L. A. Leston, P. J. D. O. Evald, "Enhancing energy quality and grid stability with improved adaptive controller for renewable energy conversion systems under weak grid conditions", *Electric Power Systems Research*, vol. 237, p. 111041, Dec. 2024, doi:10.1016/j.epsr.2024.111041.

[9] M. Ali, A. A. Alhussainy, F. Hariri, S. Alghamdi, Y. A. Alturki, "Performance Assessment of Current Feedback-Based Active Damping Techniques for Three-Phase Grid-Connected VSCs with LCL Filters", *Mathematics*, vol. 13, no. 16, p. 2592, Aug. 2025, doi:10.3390/math13162592.

[10] I. Podlubny, "Fractional-order systems and $PI^{\lambda}D^{\mu}$ controllers", *IEEE Transactions on Automatic Control*, vol. 44, no. 1, pp. 208–214, Jan. 1999, doi:10.1109/9.739144.

[11] D. Mishra, P. C. Sahu, R. C. Prusty, S. Panda, "A fuzzy adaptive fractional order-PID controller for frequency control of an islanded microgrid under stochastic wind/solar uncertainties", *International Journal of Ambient Energy*, vol. 43, no. 1, pp. 4602–4611, Apr. 2022, doi:10.1080/01430750.2021.1914163.

[12] M. Abdollahzadeh, H. Mollaee, S. M. Ghamari, F. Khavari, "Design of a novel robust adaptive neural network-based fractional-order proportional-integrated-derivative controller on DC/DC Boost converter", *The Journal of Engineering*, vol. 2023, no. 4, p. e12255, Apr. 2023, doi:10.1049/tje2.12255.

[13] R. Kashfi, S. Balochian, M. Alishahi, "Design of a optimal robust adaptive neural network-based fractional-order PID controller for H-bridge single-phase inverter", *Applied Soft Computing*, vol. 166, p. 112142, Nov. 2024, doi:10.1016/j.asoc.2024.112142.

[14] O. Jafarzadeh, S. A. M. Ghasemi, S. M. Zahrai, R. Sabetahd, A. Mohammadzadeh, R. Vafaei Poursorkhabi, "Design of an Online Adaptive Fractional-Order Proportional-Integral-Derivative Controller to Reduce the Seismic Response of the 20-Story Benchmark Building Equipped with an Active Control System", *International Journal of Intelligent Systems*, vol. 2024, no. 1, p. 5648897, Aug. 2024, doi:10.1155/2024/5648897.

[15] Y. Wang, J. Peng, K. Zhu, B. Chen, H. Wu, "Adaptive PID-fractional-order nonsingular terminal sliding mode control for cable-driven manipulators using time-delay estimation", *International Journal of Systems Science*, vol. 51, no. 15, pp. 3118–3133, Aug. 2020, doi:10.1080/00207721.2020.1808732.

[16] A. Ansarian, M. J. Mahmoodabadi, "Multi-objective optimal design of a fuzzy adaptive robust fractional-order PID controller for a nonlinear unmanned flying system", *Aerospace Science and Technology*, vol. 141, p. 108541, Oct. 2023, doi:10.1016/j.ast.2023.108541.

[17] A. K. Sahin, B. Cavdar, M. S. Ayas, "An adaptive fractional controller design for automatic voltage regulator system: Sigmoid-based fractional-order PID controller", *Neural Computing and Applications*, vol. 36, no. 23, pp. 14409–14431, May 2024, doi:10.1007/s00521-024-09816-6.

[18] B. Abdollahzadeh, N. Khodadadi, S. Barshandeh, P. Trojovský, F. S. Gharehchopogh, E.-S. M. El-kenawy, L. Abualigah, S. Mirjalili, "Puma optimizer (PO): a novel metaheuristic optimization algorithm and its application in machine learning", *Cluster Computing*, vol. 27, no. 1, pp. 5235–5283, Jan. 2024, doi:10.1007/s10586-023-04221-5.

[19] R. Cardoso, R. F. D. Camargo, H. Pinheiro, H. A. Gründling, "Kalman filter based synchronisation methods", *IET Generation, Transmission and Distribution*, vol. 2, no. 4, pp. 542 – 555, Jul. 2008, doi:10.1049/iet-gtd:20070281.

[20] A. Reznik, M. G. Simoes, A. Al-Durra, S. M. Muyeen, "LCL filter design and performance analysis for grid-interconnected systems", *IEEE Transactions on Industry Applications*, vol. 50, no. 2, pp. 1225–1232, Apr. 2013, doi:10.1109/TIA.2013.2274612.

[21] P. J. D. O. Evald, R. V. Tambara, H. A. Gründling, "A direct discrete-time reduced order robust model reference adaptive control for grid-tied power converters with LCL filter", *Open Journal of Power Electronics*, vol. 25, no. 3, pp. 361–372, Sep. 2020, doi:10.18618/REP.2020.3.0039.

[22] S. Dey, S. Banerjee, J. Dey, "Design and performance analysis of optimized fractional order PID controller for magnetic levitation system", *in IEEE 4th International Conference on Computing, Power and Communication Technologies (GUCON)*, pp. 1–6, IEEE, Sep. 2021, doi:10.1109/GUCON50781.2021.9574026.

[23] K. Oprzedkiewicz, W. Mitkowski, E. Gawin, "An estimation of accuracy of Oustaloup approximation", *in Challenges in Automation, Robotics and Measurement Techniques: Proceedings of AUTOMATION-2016*, pp. 299–307, Springer, 2016, doi:10.1007/978-3-319-29357-8_27.

[24] P. A. Ioannou, J. Sun, *Robust adaptive control*, vol. 1, PTR Prentice-Hall Upper Saddle River, NJ, EUA, 1996.

[25] P. J. D. O. Evald, G. V. Hollweg, W. B. da Silveira, D. M. C. Milbradt, R. V. Tambara, H. A. Gründling, "Performance comparison of discrete-time robust adaptive controllers for grid-tied power converters under unbalanced grids", *e-Prime-Advances in Electrical Engineering, Electronics and Energy*, vol. 4, p. 100143, Jun. 2023, doi:10.1016/j.prime.2023.100143.

## AUTHOR'S CONTRIBUTIONS

**C.T.G.B.Oliveira**: Data Curation, Investigation, Methodology, Software, Visualization, Writing – Original Draft. **W.B.Silveira**: Resources, Software, Writing – Review & Editing. **P.J.D.O.EVALD** Conceptualization, Methodology, Project Administration, Supervision, Validation, Visualization, Writing – Review & Editing.

## PLAGIARISM POLICY

This article was submitted to the similarity system provided by Crossref and powered by iThenticate – Similarity Check.

## DATA AVAILABILITY

The data used in this research is available in the body of the document.

## BIOGRAPHIES

**Cairo Túlio Gomes Barros Oliveira** is an Automation Engineering student from the Federal University of Pelotas (UFPel). His main research areas are power electronics control applications and meta-heuristic optimization.

**Wagner Barreto da Silveira** received the B.Sc. and M.Sc. in Electrical Engineering at the Federal University of Santa Maria (UFSM) in 2018 and 2021, respectively. Currently, he is a Ph.D. candidate in Electrical Engineering at UFSM.

**Paulo Jefferson Dias de Oliveira Evald** received the B.Sc. in Automation Engineering (2016) and M.Sc. in Computer Engineering (2018), both from the Federal University of Rio Grande (FURG), and a Ph.D. in Electrical Engineering (2021) from UFSM. Since 2022, he has been a Professor at the UFPel and a member of the Intelligent Systems and Control Group (ISCG/UFPel).